



## Article

# Crater Detection and Population Statistics in Tianwen-1 Landing Area Based on Segment Anything Model (SAM)

Yaqi Zhao and Hongxia Ye \*

Key Laboratory for Information Sciences of Electromagnetic Waves (MoE), Fudan University, Shanghai 200433, China; 21210720309@m.fudan.edu.cn

\* Correspondence: yehongxia@fudan.edu.cn

**Abstract:** Crater detection is useful for research into dating a planetary surface's age and geological mapping. The high-resolution imaging camera (HiRIC) carried by the Tianwen-1 rover provides digital image model (DIM) datasets with a resolution of 0.7 m/pixel, which are suitable for detecting meter-scale craters. The existing deep-learning-based automatic crater detection algorithms require a large number of crater annotation datasets for training. However, there is currently a lack of datasets of optical images of small-sized craters. In this study, we propose a model based on the Segment Anything Model (SAM) to detect craters in Tianwen-1's landing area and perform statistical analysis. The SAM network was used to obtain a segmentation mask of the craters from the DIM images. Then non-circular filtering was used to filter out irregular craters. Finally, deduplication and removal of false positives were performed to obtain accurate circular craters, and their center's position and diameter were obtained through circular fitting analysis. We extracted 841,727 craters in total, with diameters ranging from 1.57 m to 7910.47 m. These data are useful for further Martian crater catalogs and crater datasets. Additionally, the crater size–frequency distribution (CSFD) was also analyzed, indicating that the surface ages of the Tianwen-1 landing area are ~3.25 billion years, with subsequent surface resurfacing events occurring ~1.67 billion years ago.

**Keywords:** Mars; crater detection; Tianwen-1; segmentation; segment anything model



**Citation:** Zhao, Y.; Ye, H. Crater Detection and Population Statistics in Tianwen-1 Landing Area Based on Segment Anything Model (SAM). *Remote Sens.* **2024**, *16*, 1743. <https://doi.org/10.3390/rs16101743>

Academic Editor: Jonathan H. Jiang

Received: 30 March 2024

Revised: 1 May 2024

Accepted: 9 May 2024

Published: 14 May 2024



**Copyright:** © 2024 by the authors. Licensee MDPI, Basel, Switzerland. This article is an open access article distributed under the terms and conditions of the Creative Commons Attribution (CC BY) license (<https://creativecommons.org/licenses/by/4.0/>).

## 1. Introduction

China's first Mars exploration mission, Tianwen-1, was launched on 23 July 2020, with the aim of completing orbital, landing, and roving tasks. The high-resolution imaging camera (HiRIC) [1] carried by the Tianwen-1 orbiter provided detailed images of the landing area. The landing area is dotted with numerous craters, which can offer crucial information about the evolution of the landing region. Craters, as one of the most prominent features on the planetary surface, play a key role in planetary science. The distribution of craters provides valuable clues for revealing the aging process of geological structures [2,3] and is also one of the important factors in selecting landing sites for planetary probes [4]. Calculating the size–frequency distribution of craters is a primary method for estimating the surface age of celestial bodies [5,6], making it a key technique in planetary geological research. Therefore, the automatic segmentation and statistical analysis of the features of Martian surface craters are crucial in Martian exploration missions. Traditional methods [2,7] rely on planetary scientists manually labeling craters on remote sensing images, which is time-consuming and labor-intensive, and cannot detect craters in real time. Therefore, an efficient, accurate, and unsupervised method for automatic crater detection is highly necessary.

Currently, several methods for automatic crater detection have been developed, which can be roughly categorized into methods based on extraction of the morphological features and methods based on deep learning. Methods based on extraction of the morphological features utilize intuitive and simple features, such as the craters' shape or spectral characteristics, such as the Canny edge contour algorithm [8], the Hough transform [9],

and template matching [10]. Yang et al. [8] used a multi-scale Canny operator to detect the edges of craters. However, variations in the illumination conditions between different images may affect the performance of edge detection, resulting in suboptimal crater detection. Leroy et al. [11] utilized template matching and probability volume analysis to identify Martian craters larger than 5 pixels (an image resolution of 250 m/pixel). However, the experimental scenarios were relatively simple, with mostly regular circular craters. Galloway et al. [12] investigated the impact of preprocessing via Canny edge detection on the performance of the Hough transform, finding that edge detection significantly affected the performance of the Hough transform, and they considered the Hough transform to be a more practical method than edge detection. However, their approach requires computing gradients for each edge pixel, which is time-consuming, and they did not test the performance when detecting multiple-sized craters in larger images. These methods based on the extraction of morphological features can effectively detect simple craters in small datasets. However, due to the complexity of the terrain conditions and the common occurrence of densely distributed craters in real-world scenarios, these methods exhibit relatively lower detection rates and efficiency when dealing with large-scale datasets.

To improve the efficiency of automatic crater detection, deep learning has been widely applied in crater detection tasks. Convolutional Neural Network (CNN)-based deep learning algorithms have achieved tremendous success in segmentation and detection tasks in remote sensing images [13,14]. Li et al. [15] introduced a novel encoder-decoder-based network, MarsSeg, specifically tailored for segmentation of the Martian landscape, and demonstrated its advanced performance. Silburt et al. [16] successfully used the U-Net [17,18] model and template matching algorithm to extract craters on lunar DEM images. Since the U-Net network layers they used were relatively shallow, the segmentation ability for the craters' outlines was poor. Lee et al. [19] utilized the U-Net model trained on lunar DEM images by Silburt et al. to identify and extract craters in Martian DEM images, confirming the effectiveness of the U-Net model in crater detection. In order to enhance the efficiency of crater detection and the accuracy of identifying large Martian craters, Chen et al. [20] proposed a novel CNN called MC-UNet. They incorporated average pooling and embedded channel attention into the skip-connection process between the encoder and decoder layers to identify craters in optical images of Mars. To improve the performance and accuracy of automatic crater identification, Zhao et al. [21] explored a novel embedded U-Net structure based on U-Net, named Square U-Net (SqUNet). They used the embedded U-Net architecture to replace traditional convolutional modules, successfully achieving high-precision identification and extraction of lunar DEM craters, and demonstrating high-precision test results on Martian DEM as well. However, these algorithms for automatic crater detection are supervised models, requiring many labeled crater datasets for training. The currently available global catalogs of lunar craters [2,7,22] include craters with diameters greater than 1 km, while the global catalog of Martian craters includes craters with diameters greater than 1 km [23]. The Chang'e-5's landing area has a catalog of craters with diameters larger than 200 m [24]. However, most landing areas lack a catalog of meter-sized craters. Therefore, in the absence of a crater catalog, a model that does not require additional training would be highly valuable.

In the remote sensing field, several foundational large models tailored for segmentation tasks have emerged, such as RSPrompter [25] and SAM [26]. These foundational large models are typically trained on extremely large annotated datasets, endowing them with strong generalization capabilities for segmentation tasks. Therefore, they can be easily extended to other segmentation tasks. SAM [26], in particular, is suitable for unsupervised segmentation tasks. SAM was initially designed to address a fundamental challenge in image segmentation: how to effectively identify and segment objects in images without training data that are specific to a particular task. SAM aims to create a universal model that is capable of adapting to different types and sizes of images, automatically identifying and segmenting target objects in these images, even if these objects have never been encountered by the model before. SAM networks have achieved significant success in various domains.

In the field of medical imaging, SAM has been used for the automatic identification and segmentation of structures in various medical images [27], which is particularly important in situations with a scarcity of annotated medical images. In processing remote sensing images, Giannakis et al. [28] validated the effectiveness of SAM in identifying planetary craters by providing examples from different celestial bodies and types of data. However, extracting crater targets from high-resolution planetary images remains challenging due to SAM's ability to extract any type of target from images.

The Tianwen-1 mission landed in the southern part of Utopia Planitia, located in the northern lowlands of Mars (25.1°N, 109.9°E). Tianwen-1 is a comprehensive mission aiming to study the morphology, mineralogy, spatial environment, and distribution of water ice on Mars [29]. Many researchers have conducted detailed geological surveys of the Tianwen-1 landing area, gaining a deep understanding of the geological background and evolutionary history of Utopia Planitia [30–33]. However, studies on impact craters in the Tianwen-1 landing area have only extracted partial areas or a small number of large craters for an analysis of their distribution, lacking a detailed catalog of craters in the landing area. Currently, the Tianwen-1 landing area has a catalog of craters with diameters larger than 80 m [34]. Cao et al. [35] annotated over 7000 craters larger than 1 m in three subregions of the Tianwen-1 landing area, providing labels for small-sized craters. Providing a complete catalog of meter-sized impact craters for the landing area is crucial. Understanding the distribution, quantity, size, and other important parameters of craters not only helps deepen our understanding of the geological environment near the Mars landing site but also provides important references for future scientific research and exploration missions. This study aimed to extract multi-scale craters in the landing area and make a more detailed and in-depth analysis of the age and geological evolution of the landing area.

In this work, we used SAM to identify and extract craters from the digital image model (DIM) of the Tianwen-1 landing area. The SAM was used to identify craters in the DIM and obtain their segmentation mask, and a series of postprocessing steps was performed to extract the positions and sizes of craters. Through analyzing the CSFD of the craters, we estimated their specific surface age to be approximately ~3.25 Ga, with subsequent surface resurfacing events occurring around ~1.67 Ga. The main contributions of this article are as follows:

- (a) We proposed a complete solution for automatic crater identification based on SAM, which was applied to extract craters from the DIM of the Tianwen-1 landing area.
- (b) Experiments were conducted in three subregions of the Tianwen-1 landing area, where SAM achieved a recall rate of 100%. Many new craters were detected, confirming its effectiveness in the task of crater extraction.
- (c) On the basis of the DIM of the Tianwen-1 landing area, we provided a relatively comprehensive crater dataset, including information on the position and diameter of the craters.
- (d) We analyzed the CSFD of the craters and estimated the surface age of the landing area, conducting an analysis of the geological evolution of the landing region.

The structure of this article is as follows: Section 2 introduces the complete process of using SAM to extract craters from the DIM of the Tianwen-1 landing area. Section 3 describes the experimental results of SAM on the lunar crater dataset. Section 4 presents the results of crater extraction, including an analysis of the number of craters extracted, an analysis of the craters' size and distribution frequency, and an explanation of the catalog of craters. Section 5 discusses the limitations of the study and outlines future work. Finally, Section 6 draws some conclusions.

## 2. Materials and Methods

We utilized the DIM data of the Tianwen-1 landing area captured by the high-resolution imaging camera (HiRIC) [1] installed on the Tianwen-1 orbiter. The resolution is 0.7 m per pixel, allowing for the detection of small-sized craters at the meter scale. The

complete process of extracting craters from the Tianwen-1 landing area's DIM consisted of three steps. Firstly, preprocessing of the data was conducted by performing multi-scale cropping and down-sampling of the Tianwen-1 landing area DIM to generate a multi-scale dataset. Next, the SAM was applied to segment the newly generated multi-scale dataset [26]. Subsequently, each segmented mask was analyzed, non-circular masks were filtered out, and circular fitting was applied to the filtered mask edges. Next, deduplication and removal of false positives were performed on the information on the craters extracted from the multi-scale dataset. Finally, the pixel coordinates of the impact craters' centers were converted to latitude and longitude coordinates.

### 2.1. Data Preprocessing

Figure 1a shows the DIM of the entire landing area, which was obtained by stitching together 15 DIMs with a pixel size of  $28,583 \times 42,869$  on the basis of their latitude and longitude. The pixel size of DIM images for the entire landing area is  $85,749 \times 214,345$  (<https://moon.bao.ac.cn/web/zhmanager/mars1>, accessed on 3 August 2021). Figure 1b shows the details of one image, where some craters of different sizes can be seen. Due to the different scales of the craters in the images, we adopted a multi-scale cropping strategy, which helped the network model adapt better to the objects' size. We performed overlapping cropping using five different scales with cropping sizes of  $1024 \times 1024$ ,  $2048 \times 2048$ ,  $4096 \times 4096$ ,  $8192 \times 8192$ , and  $16,384 \times 16,384$ , corresponding to overlap sizes of 128, 256, 512, 1024, and 2048, respectively. The corresponding pixel diameter range of the main craters detected were 2~100, 4~200, 8~400, 16~800, and 32~1600, respectively. This approach allowed for the extraction of as many craters of all sizes as possible.

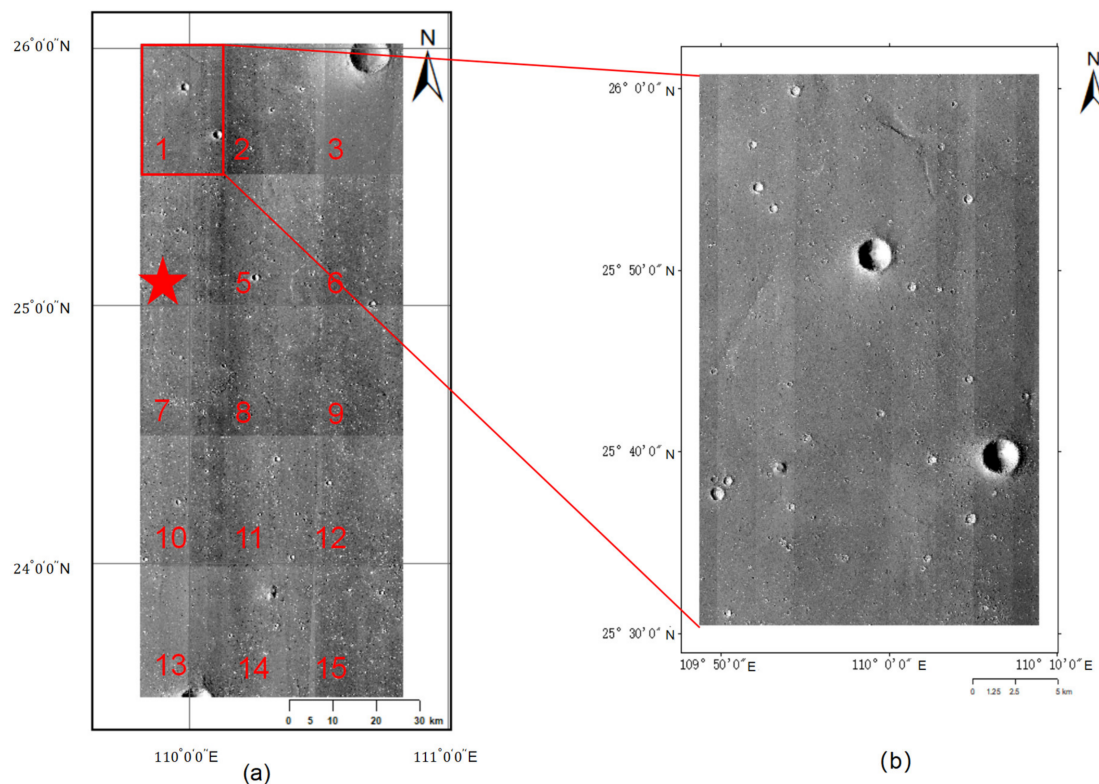


**Figure 1.** Digital image map (DIM) of Tianwen-1's landing area. (a) The 15 DIMs of the landing area. The red star in the image represents the landing location of the Zhurong rover. (b) DIM of the first region in the landing area (HX1\_GRAS\_HIRIC\_DIM\_0.7\_0001\_254537N1095850E\_A).

### 2.2. SAM

The SAM [26] is an advanced deep learning image segmentation model that has been trained on a total of over 1.1 billion masks from more than 11 million images [26],

demonstrating exceptional image segmentation capabilities. The model consists of three main components: a prompt encoder, an image encoder, and a lightweight mask decoder. The image is processed through the image encoder. The prompts, such as points, boxes, masks, or text, are transformed into a form that is understandable by the model through the prompt encoder. The mask decoder receives representations of the prompts and images to produce plausible masks.

Figure 2 shows the data flow of the SAM's network in generating crater masks from the DIM's outputs. The default parameters of the SAM network were used. First, the image was preprocessed by resizing its longest side to 1024 while maintaining the aspect ratio and then normalizing it. The image encoder used was the Vision Transformer (ViT) [36], which treated the image as a sequence of patches and captures complex relationships between these patches using a self-attention mechanism. After preprocessing, the image was segmented into patches through patch embedding, and each patch was converted into a deep feature vector. Here, patch embedding used a 2D convolution with a kernel size of  $16 \times 16$ , a stride of 16, and an output dimension of 1280, resulting in  $64 \times 64 \times 1280$  feature maps. Next, position encoding was added to help the model understand the spatial arrangement of the objects in the image. Then these vectors were processed using the transformer architecture [37] to enhance the features' representation and obtain high-dimensional image embeddings. Finally, a convolutional neural network (CNN) was used for reducing the dimensionality and adjustment of the channel for the segmentation task. The prompt encoder can encode points, boxes, masks, and text, but in this case, automatic segmentation was adopted. In this form,  $32 \times 32$  independent prompt points were evenly distributed across the image region, and the prompt points contained information on the location. These points were divided into 16 batches, each with 64 points. Through the mask decoder, the masks and the corresponding confidence IOU prediction values were generated. The masks were filtered using the box non-maximum suppression (Box NMS) [26] technique to retain the most relevant bounding boxes and eliminate redundant ones, resulting in 112 masks. The results included the following information:

- Segmentation masks and the area of each mask;
- Boundary boxes for each mask;
- A quality score (ranging from 0 to 1) for the boundary box of each mask, measuring the reliability of the mask;
- A stability score (ranging from 0 to 1) for each mask, assessing the stability of the mask at different input coordinates.

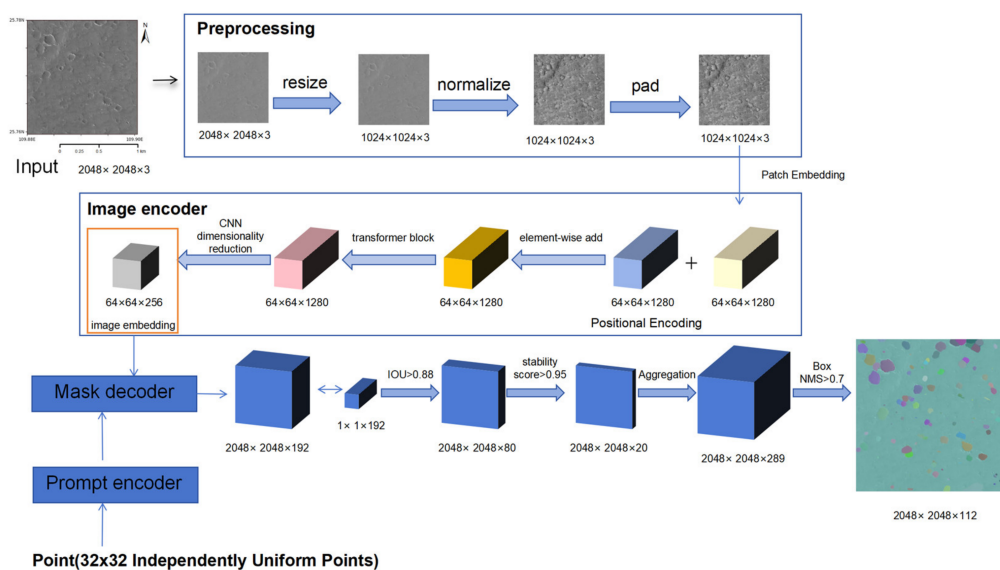


**Figure 2.** Network structure of the SAM for the automatic identification of craters (Different colors in the output image represent different segmentation targets).

In summary, SAM is suitable for crater detection tasks, as it can identify craters and estimate the size of craters by providing direct information about the mask's edges and region. Figure 3 illustrates an example of using SAM to identify craters in the DIM of the Tianwen-1 landing area, in which different colors represent different segmented objects. Despite not being specifically trained for high-resolution images of Mars, SAM appeared to capture all major features in the image, demonstrating its effectiveness in crater detection. Additionally, SAM could identify craters and provide information about the masks' edges and regions for estimations of the craters' size, offering significant advantages in creating crater datasets.

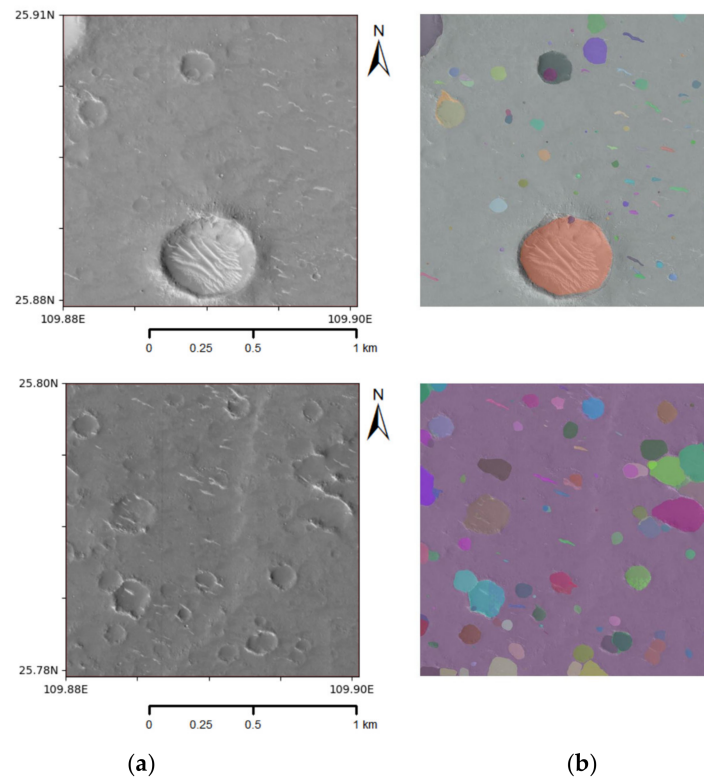


**Figure 3.** Segmented images from SAM (Different colors in the output image represent different segmentation targets). (a) DIM of the landing area. (b) Segmented images outputted by SAM.

### 2.3. Crater Extraction

The main process for extracting craters from the DIM images of the Tianwen-1 landing area was as follows:

- (a) Using SAM model to obtain segmentation masks for DIM images of different sizes;
- (b) Filtering out non-circular edges from the segmented edges;
- (c) Performing circular fitting with the edges of the segmentation masks;
- (d) Removing duplicates and false circles;
- (e) Converting pixel coordinates to geographic coordinates.

#### 2.3.1. Circular Metrics

The above SAM extracts segmentation masks with different morphological features from input images. We used the “findContours” function in OpenCV [38] to obtain the coordinates of edge pixels in the mask. Most craters have a circular shape, so we needed to filter out the non-circular masks. We defined  $n$  as a measure to evaluate the circularity of each mask, and the formula was defined as follows [39].

$$n = \frac{C}{P} = \frac{2\sqrt{\pi A}}{P} \quad (1)$$

Here,  $A$  is the area of the mask (number of pixels), and  $P$  is the sum of distances between any two adjacent pixels on the boundary.

This study aimed to create a dataset of craters, including the centers' coordinates and radius, and only regular circular craters were considered. Therefore, a circularity threshold parameter was used to filter irregular circular craters. Figure 4 shows the circularity statistics of all the extracted objects in the dataset. We found that 57% of the objects had a circularity above 0.75. Subsequently, a circularity threshold of 0.75 was set to filter irregular circular craters. Objects with a circularity greater than 0.75 were retained for subsequent circular fitting. A detailed analysis for this threshold is in Section 3.2.

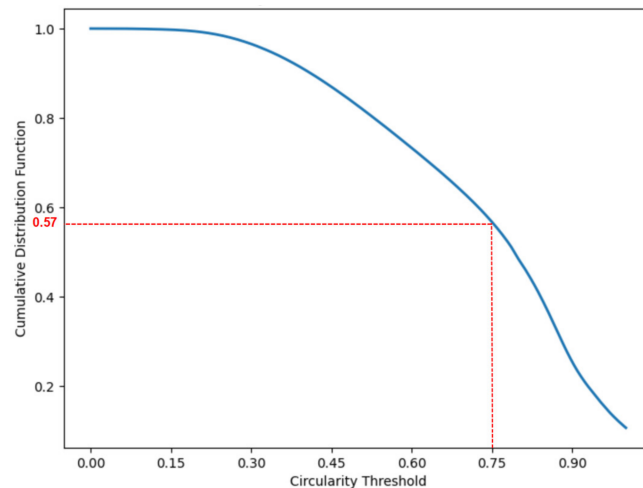


**Figure 4.** Cumulative distribution curve of the circularity of objects segmented using SAM.

Figure 5 shows the images before (Figure 5a) and after (Figure 5b) removing non-circular masks. It can be observed that almost all the non-circular masks (green) were removed, while the remaining circular masks (red) proceeded to the subsequent circular fitting step.

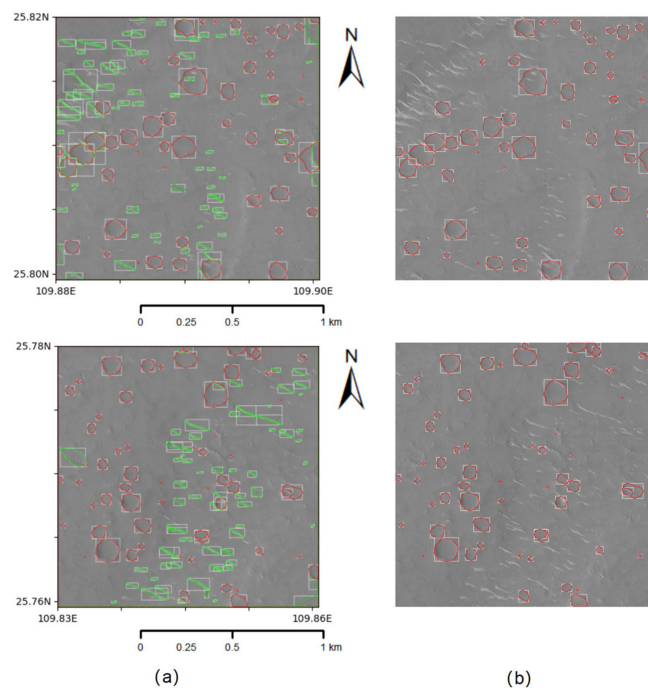


**Figure 5.** Non-circular filtering of the segmentation objects generated by SAM (Green represents non-circular segmentation targets, while red represents circles). (a) Segmentation results outputted by SAM. (b) Results after filtering non-circular objects.

### 2.3.2. Circular Fitting

We used the least squares method to perform circular fitting on the edges of the remaining masks. Initially, an estimation of the circle's center and radius is made for each mask. The initial estimation of the center was the mean of the point set, and the initial estimation of the radius was the average distance from the points to that mean. The least squares method was then utilized to minimize the distance errors between the fitted circle and the actual edge points, providing the optimal fit for the circle's center and radius. The formula for the distance error is as follows:

$$S(x_0, y_0, r) = \sum_{i=1}^n [(x_i - x_0)^2 + (y_i - y_0)^2 - r^2]^2 \quad (2)$$

Here,  $x_i$  and  $y_i$  represent the coordinates of each edge point,  $(x_0, y_0)$  represents the central coordinates of the fitted circle, and  $r$  represents the radius of the fitted circle. Finally, the parameter information of the fitted circle was updated in the data for further analysis and statistics.

Figure 6 illustrates the images before (a) and after (b) circular fitting. It can be observed that the fitted circles accurately represent the size and position of the craters in the results of extraction across different sizes.

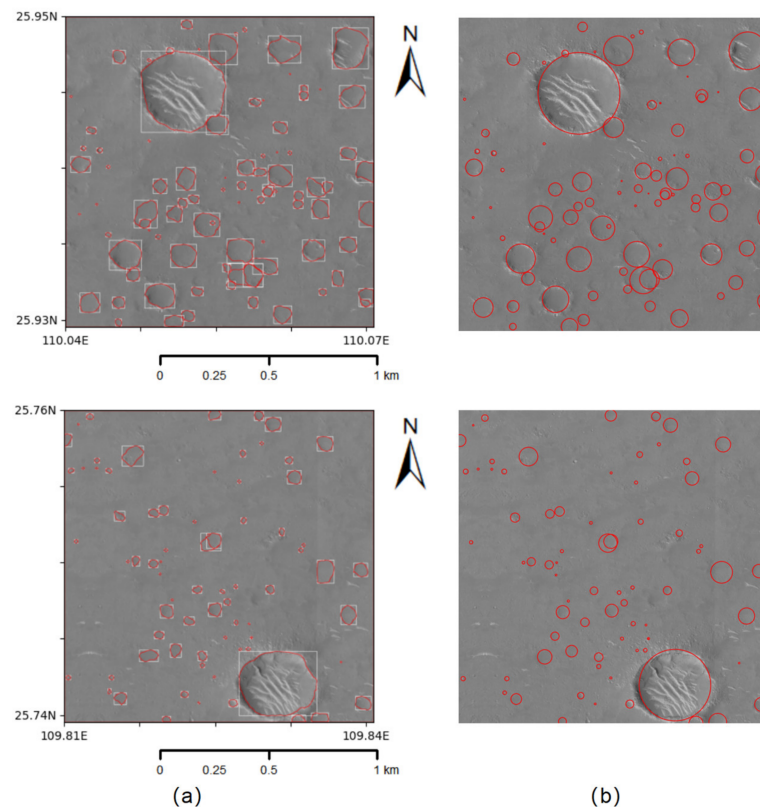


**Figure 6.** Circular fitting of the mask edges extracted by SAM: (a) before circular fitting; (b) after circular fitting.

### 2.3.3. Remove of Duplicates and False Craters

We merged the segmentation results of datasets cropped at different scales back into the original large image. Figure 7 shows the distribution of the size and quantity of craters at different cropping sizes. The results indicated that with an increase in the cropping size, the range of the diameters of successfully extracted craters also expanded. This further validated the necessity of multi-scale cropping for extracting craters of various sizes. Figure 8 displays the craters extracted from datasets cropped at five different sizes.

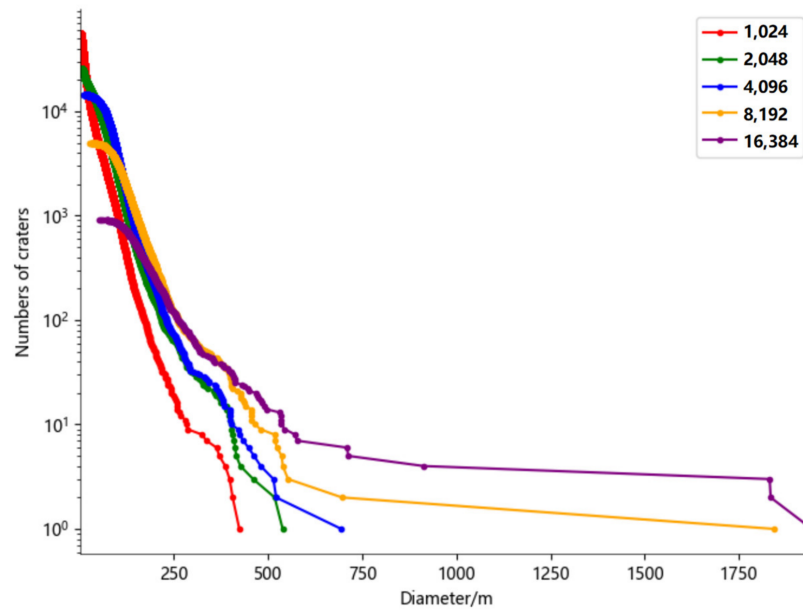


**Figure 7.** The distribution of crater sizes and quantities resulting from different cropping sizes.

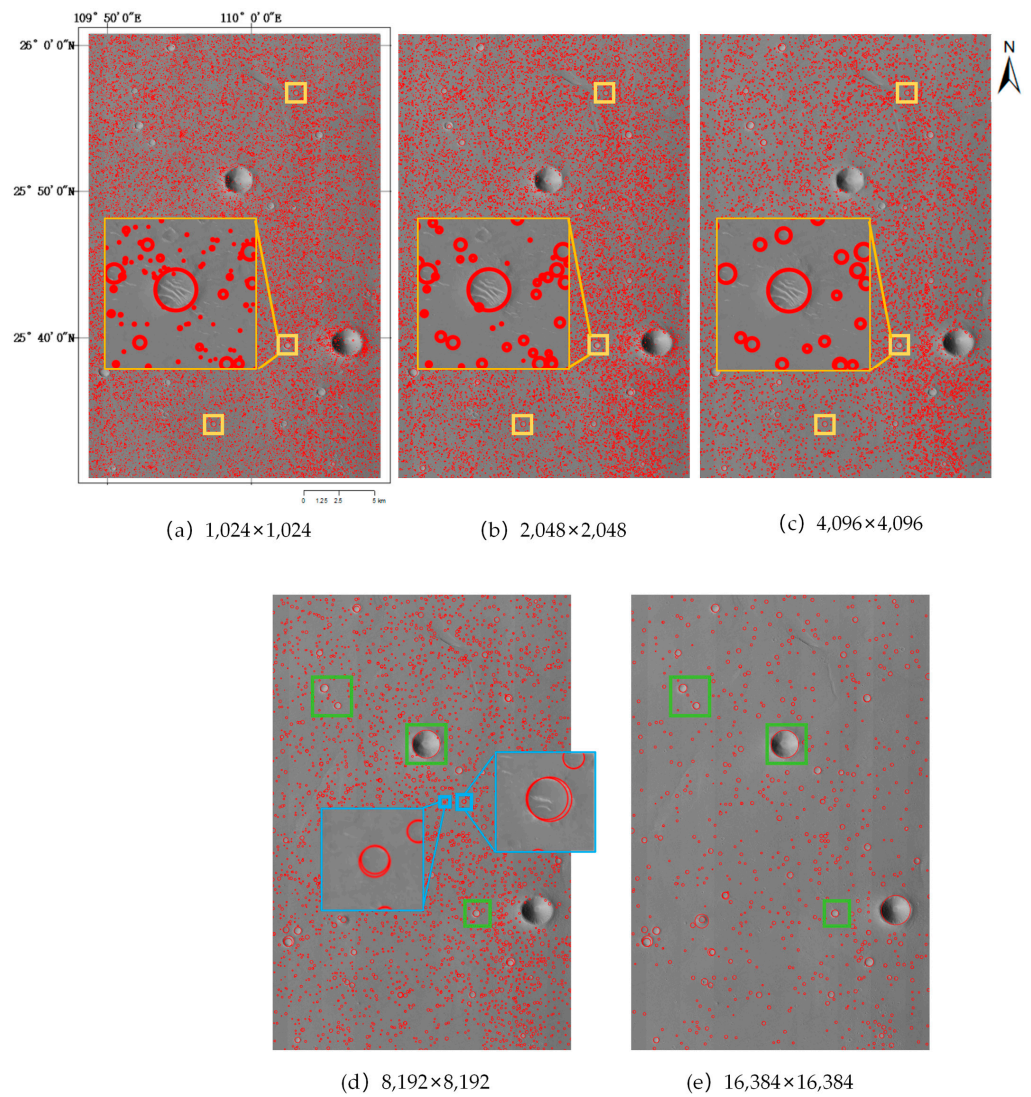


**Figure 8.** Results of extracting craters from datasets with different cropping sizes.

However, there are duplicates in the results of extracting crater at different sizes. For example, craters highlighted in the yellow boxes in Figure 8a–c, and the green boxes in Figure 8d,e show duplicates. Additionally, due to overlapping during the cropping process, craters extracted from datasets with the same cropping size may also have a partial overlap, as exemplified by the crater highlighted in the blue boxes in Figure 8d. To ensure the uniqueness of the final crater data extracted, we performed a deduplication process. A crater's information was recorded as  $(x_i, y_i, r_i)$ , and another crater's information was labeled as  $(\hat{x}_j, \hat{y}_j, \hat{r}_j)$ . If two craters satisfied Equations (3) and (4), they were labeled as duplicate craters and removed. Here, to improve the computational efficiency, we only calculated the distance between a crater and other craters located in an  $8192 \times 8192$  grid centered at the crater's center.

$$\left( (x_i - \hat{x}_j)^2 + (y_i - \hat{y}_j)^2 \right) / \min(r_i, \hat{r}_j)^2 < D_{x,y} \quad (3)$$

$$\text{abs}(r_i - \hat{r}_j) / \min(r_i, \hat{r}_j) < D_r \quad (4)$$

Here,  $D_{x,y} = 1.8$  and  $D_r = 1.0$  are hyperparameters [16].

Upon examining the images after deduplication, we observed that there was some texture at the bottom of the crater. This type of texture is formed by transverse aeolian ridges (TARs) resulting from weathering [40]. The shaded areas formed by the TARs exhibit circular features in the optical images and were consequently incorrectly identified as craters, as shown by the green crater in Figure 9a. To address this issue, we introduced an intersection over union (IOU) threshold, defined as in Equation (5)

$$\text{IOU} = \frac{A \cap B}{A \cup B} \quad (5)$$

where  $A$  and  $B$  represent the areas of the two circles. Figure 9a shows the result with the IOU set to 0.8, and Figure 9b shows the result with the IOU set to 0.7. It can be seen that when the IOU was 0.7, false craters were removed. Therefore, we set the IOU threshold to 0.7. If the IOU was greater than 0.7, the smaller one of the two circles was deemed to be a pseudo-crater. Figure 9b displays the image after the removal of these false craters.

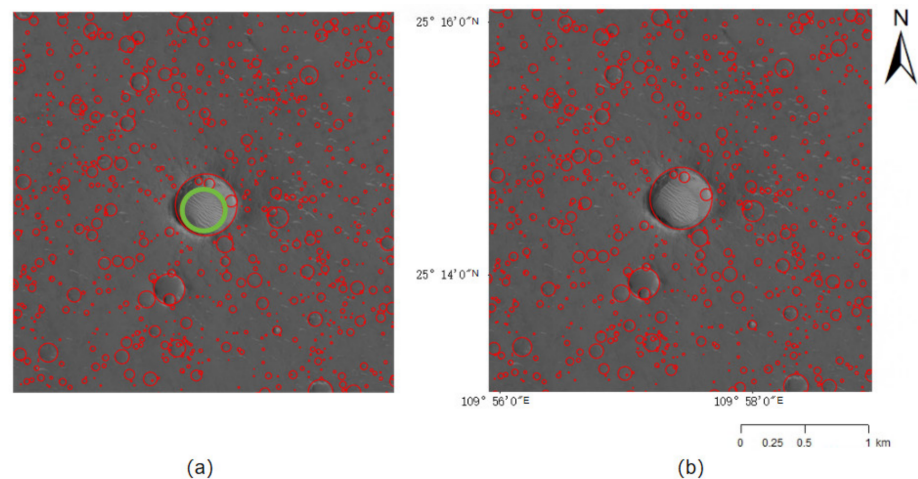


**Figure 9.** (a) Before removing false craters (IOU = 0.8). (b) After removing false craters (IOU = 0.7).

#### 2.3.4. Transformation of Coordinates

We merged the segmentation results of datasets cropped at different scales back into the original large image. Finally, we needed to convert the pixel coordinates of the craters to latitude and longitude coordinates using Equations (6) and (7).

$$la = \frac{x}{L}(La_r - La_l) + La_l \quad (6)$$

$$lo = Lo_l - \frac{y}{H}(Lo_l - Lo_r) \quad (7)$$

Here,  $(la, lo)$  and  $(x, y)$  represent the latitude and longitude coordinates and pixel coordinates of a point, respectively.  $L$  and  $H$  are the given pixel length and height of the cropping area, and  $(La_l, Lo_l)$  and  $(La_r, Lo_r)$  are the latitude and longitude coordinates of the upper left and lower right corners of the cropping area, respectively.

### 3. Experimental Results and Analysis

This section presents the experimental results of SAM in extracting Martian craters, including the evaluation metrics and an analysis of the results. The experiments verified the effectiveness of SAM in the task of crater extraction.

#### 3.1. Evaluate Metrics

To evaluate the effectiveness of SAM in the task of crater extraction, we used the precision  $P$  and recall  $R$  to measure the accuracy of the model in terms of Equations (8) and (9)

$$P = T_p / (T_p + F_p) \quad (8)$$

$$R = T_p / (T_p + F_n) \quad (9)$$

where  $T_p$  are true positives, representing the correctly identified craters;  $F_p$  are false positives, representing the craters in the results of prediction that do not match the real craters; and  $F_n$  are false negatives, representing missed craters. Here, we were more concerned about the number of detectable craters, so we cared more about the recall rate.

#### 3.2. Experimental

To verify the effectiveness of SAM in extracting craters, we conducted validation experiments using the crater catalog annotated by Cao et al. [35] in three subregions of the landing area as labels. As shown in Figure 10, the three areas had areas of  $10 \times 20$ ,  $20 \times 10$ , and  $20 \times 10 \text{ km}^2$ , with the centers located at  $(110^\circ 2' \text{E}, 25^\circ 41' \text{N})$ ,  $(110^\circ 18' \text{E}, 24^\circ 56' \text{N})$ , and  $(110^\circ 8' \text{E}, 24^\circ 24' \text{N})$ , respectively.

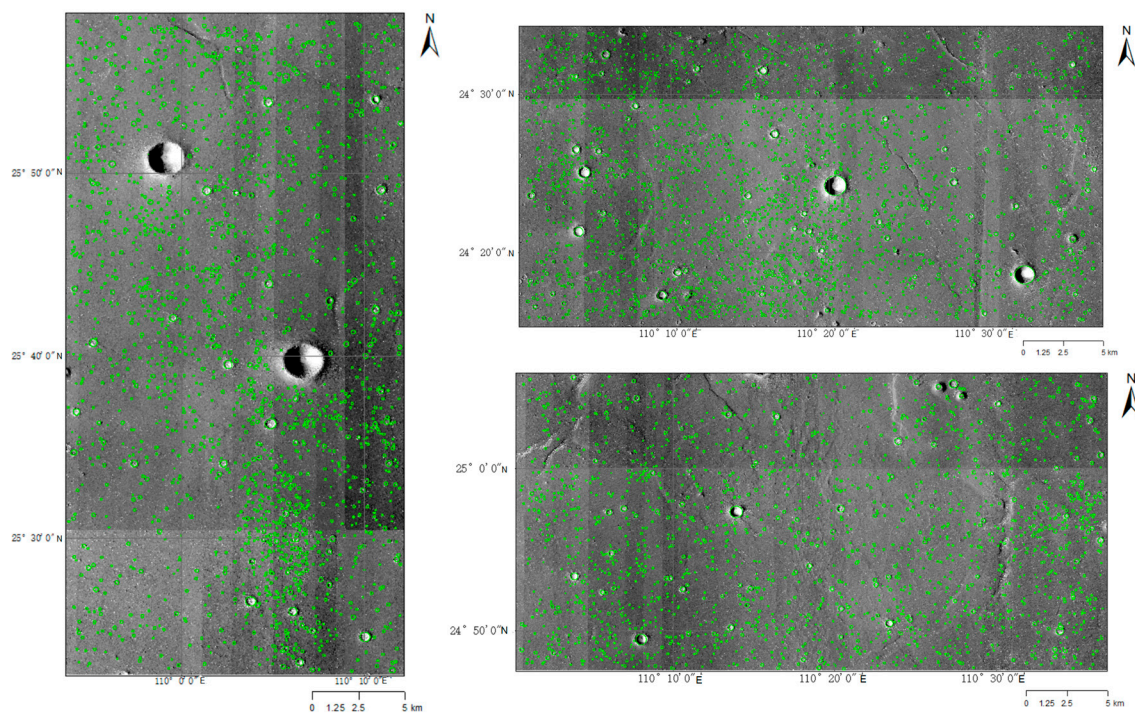


Figure 10. Crater labels for the three subregions of the landing area.

First, we evaluated the results of applying different circularity threshold filters to the craters extracted from one of the subregions. The experimental results are shown in Table 1. According to the results in Table 1, when the circularity threshold was set to less than or equal to 0.75, the recall was 1, indicating that all craters in the ground truth were detected. However, the precision significantly decreased when the circularity threshold was less than 0.75, suggesting that many non-crater objects were extracted. On the other hand, when the circularity threshold was greater than 0.75, the recall decreased significantly, indicating that many craters were missed. Since our goal was to detect as many craters as possible, we set the circularity threshold to 0.75. To verify the robustness of the method, we calculated the precision metrics of three subregions separately, and the results are shown in Table 2. The results indicated that the recall rate was 1 in each subregion, indicating that the method extracted all the craters from the labels, demonstrating the method's strong robustness in effectively extracting craters.

**Table 1.** The results of different circularity thresholds on the dataset.

Circularity Threshold		0.5	0.55	0.6	0.65	0.7	0.75	0.8	0.85	0.9	0.95
Metrics	R	1	1	1	1	1	1	92.7%	79.7%	56.8%	43.8%
	P	2.8%	3.0%	3.2%	3.4%	3.7%	4.7%	4.8%	6.1%	9.1%	13.8%

**Table 2.** The metric results for the three subregions.

Central Positions of the Subregions		110°2'E, 25°41'N	110°18'E, 24°56'N	110°8'E, 24°24'N
Metrics	R	1	1	1
	P	3.5%	4.7%	3.8%

We then compared several models, namely MC-UNet [20], ERU-Net [41], UNet++ [42], and DeepMoon [16]. These network models are relatively new and competitive architectures in the field of crater detection. The experimental results are shown in Table 3, from which it can be seen that SAM, as a model that can extract craters without training, achieved a 100% recall rate compared with several supervised models. However, the precision was lower. We conducted an analysis of the reasons and found that SAM extracted 58,724 craters, but there were only 2103 craters with the crater label. This means that we extracted many new craters, leading to a higher  $F_p$  when calculating precision; hence the calculated precision was lower.

**Table 3.** Comparison of different competing models on the datasets.

Model		SAM	MC-UNet	ERU-Net	U-Net++	DeepMoon
Metrics	R	1	89.2%	88.1%	86.3%	76.3%
	P	3.5%	80.1%	82.3%	81.5%	91.6%

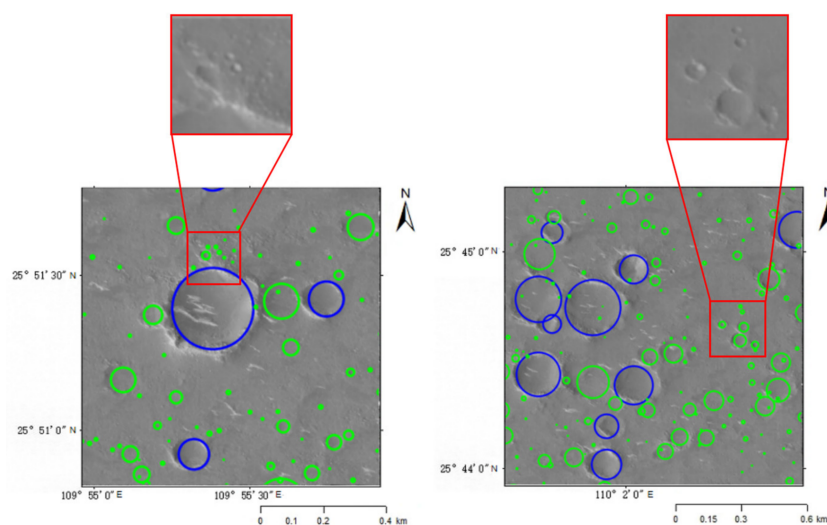
Next, we conducted a statistical analysis of the results of extraction for the three subregions, and the statistical results are shown in Table 4. The results indicated that the size range of the craters we extracted was much wider, and the number of extracted craters was significantly greater than the number of craters in the labels.

Figure 11 shows the extraction results of two small regions. The blue circles represent the craters matching the labels, while the green circles represent newly extracted craters. Compared with the craters in the ground truth, the craters extracted by SAM exhibited a wider size distribution, and SAM could extract overlapping craters. The extracted craters in the red boxes indicate that SAM identified some craters with higher degrees of edge

degradation. These results validated the high performance of SAM in the task of detecting impact craters.

**Table 4.** The results of extraction for the three subregions.

Central Positions of the Subregions	110°2'E, 25°41'N		110°18'E, 24°56'N		110°8'E, 24°24'N	
	GT	SAM	GT	SAM	GT	SAM
Size range (m)	12.1–567.9	1.9–1943.2	1.9–1300.9	1.9–1367.4	12.2–733.9	1.6–744.0
Quantity	2103	58,724	3135	65,477	2084	53,610



**Figure 11.** The results of extracting craters in two small regions.

#### 4. Statistics and Distribution of The Landing Area's Crater

This section introduces the results of crater extraction, including an analysis of the number of extracted craters, an analysis of the craters' size and distribution frequency, and an explanation of the crater catalog.

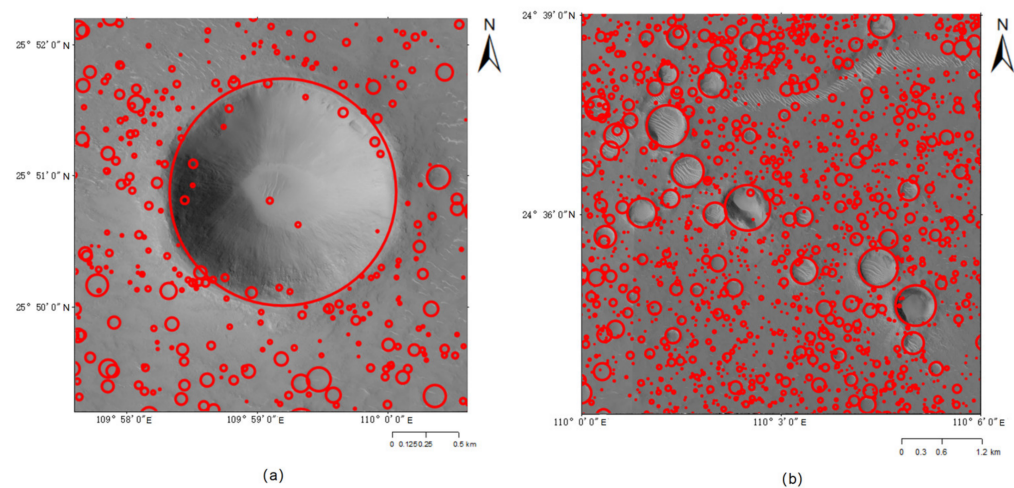
##### 4.1. Counting the Craters

We performed crater identification and extraction on 15 DIM images, and the extracted results are shown in Table 5. According to the statistics, we extracted a total of 841,727 craters in the entire landing area, with diameters ranging from 1.57 m to 7910.47 m. Figure 12 shows the results of crater identification for two subregions from different DIM images. Figure 12a demonstrates that small craters within a large crater could also be detected, while Figure 12b shows that multiple craters of different scales were detected as well.

Additionally, we performed statistical analysis on the extracted craters, categorizing them on the basis of their diameter into different ranges and plotting the crater count for each range, as shown in Figure 13a. We can see that the number of craters with diameters less than 30 m exceeded  $10^5$ , accounting for approximately 73% of the total. Craters with diameters in the range of 30–60 m constituted around 14%, while those in the range of 60–100 m accounted for approximately 8%. The proportion of craters larger than 100 m was relatively small, with a total of 40,932 craters. These findings indicated that within the landing area, small-sized craters are widely distributed. With an increase in diameter, the number of craters exhibited an exponential decline. This result is consistent with observations on the surfaces of other planets [32], as the distribution of impacting objects also follows this pattern. Additionally, over time, the number of larger craters may decrease due to erosion and geological activities [43].

**Table 5.** Statistics of the number of craters in 15 digital image models (DIMs) of the landing area.

ID	Range of Craters' Diameters (m)	Quantity (Count)	ID	Range of Craters' Diameters (m)	Quantity (Count)
HX1_GRAS_HIRIC_DIM_0.7_0001_254537N1095850E_A	1.93–1943.17	53,428	HX1_GRAS_HIRIC_DIM_0.7_0009_244453N1103919E_A	1.98–1060.23	54,670
HX1_GRAS_HIRIC_DIM_0.7_0002_254537N1101905E_A	1.57–831.91	44,950	HX1_GRAS_HIRIC_DIM_0.7_0010_241431N1095850E_A	2.14–1143.70	54,937
HX1_GRAS_HIRIC_DIM_0.7_0003_254537N1103919E_A	1.66–1528.68	51,029	HX1_GRAS_HIRIC_DIM_0.7_0011_241431N1101905E_A	1.98–1609.63	48,865
HX1_GRAS_HIRIC_DIM_0.7_0004_251515N1095850E_A	1.83–948.05	61,423	HX1_GRAS_HIRIC_DIM_0.7_0012_241431N1095850E_A	1.68–744.02	49,424
HX1_GRAS_HIRIC_DIM_0.7_0005_251515N1101905E_A	1.95–1794.37	47,557	HX1_GRAS_HIRIC_DIM_0.7_0013_234409N1095850E_A	1.64–1142.47	70,031
HX1_GRAS_HIRIC_DIM_0.7_0006_251515N1103919E_A	1.97–1240.55	69,949	HX1_GRAS_HIRIC_DIM_0.7_0014_234409N1101905E_A	1.98–1367.44	56,653
HX1_GRAS_HIRIC_DIM_0.7_0007_244453N1095850E_A	1.89–7910.47	54,900	HX1_GRAS_HIRIC_DIM_0.7_0015_234409N1103919E_A	1.57–879.72	62,522
HX1_GRAS_HIRIC_DIM_0.7_0008_244453N1101905E_A	1.95–1196.73	61,389			

**Figure 12.** Crater extraction results from different regions of the two landing areas. (a) HX1\_GRAS\_HIRIC\_DIM\_0.7\_0001\_254537N1095850E\_A. (b) HX1\_GRAS\_HIRIC\_DIM\_0.7\_0007\_244453N1095850E\_A.

We calculated the values of crater density, which is defined as the percentage of the coverage area of the craters (with a diameter  $\geq 10$  m) within a square window of  $2 \text{ km} \times 2 \text{ km}$ . Figure 13b shows the crater density map of Tianwen-1's landing region. The crater density map revealed that craters are concentrated in local regions, such as the southern and northwestern parts of the main landing region. The central-northern region exhibited lower crater densities. The area marked with a red box in the figure represents the small region where the Tianwen-1 landing site is located, and the purple star indicates the landing site, where the crater density is relatively low. The average crater density was approximately 19.3%. The maximum crater density of 100% occurred in several large craters within the main landing region.

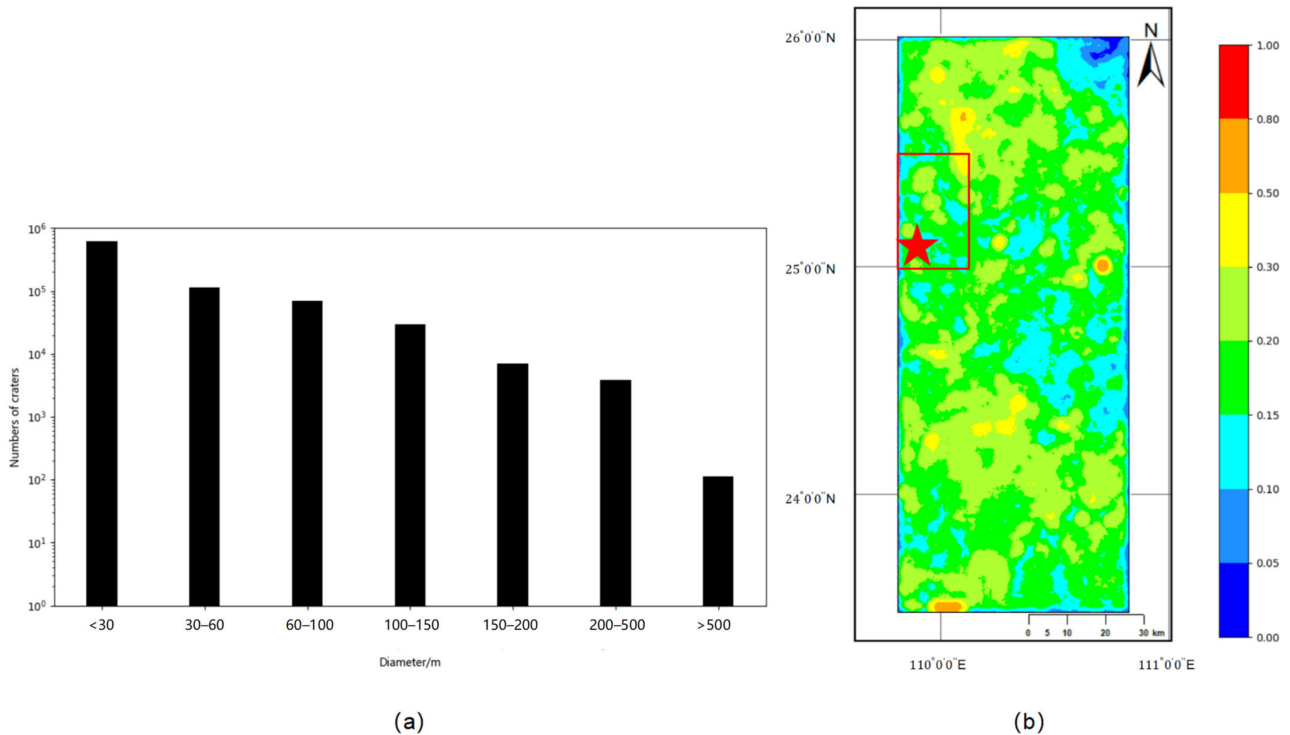


**Figure 13.** (a) Statistics of craters with different diameter ranges. (b) Map of crater density in the main landing region.

#### 4.2. Crater Size–Frequency Distribution (CSFD)

To obtain information about the surface age of the landing area, we conducted an analysis of the CSFD using the smaller-sized craters (diameter  $\geq 50$  m) detected in the landing area DIM [5]. We used the production function of Ivanov et al. [44] and the chronology function of Neukum et al. [45] for estimating the age in the landing area, resulting in a size–frequency diagram of the craters (Figure 14). The shaded regions on the map represent different Martian epochs [5,44–46], from left to right, including the Late, Middle, and Early Amazonian; Late and Early Hesperian; and Late, Middle, and Early Noachian periods.

The extracted craters with diameters greater than 1 km (black) were used to estimate the age of the landing area of Tianwen-1 as  $3.25^{+0.16}_{-0.56}$ . Age estimation was also conducted using the crater labels of the landing area in the RH\_2012 dataset [23] (green), yielding an age of  $3.21^{+0.18}_{-0.61}$ . The determinations of the age of the craters we extracted are consistent with the results obtained using the RH\_2012 dataset. According to the geological time division provided by Tanaka et al. [47], the landing area of Tianwen-1 belongs to the Late Hesperian Lowland Unit ( $3.34^{+0.02}_{-0.02}$  Ga), which is consistent with the results obtained in our study.

However, estimation of the age of the craters with diameters ranging from 50 to 800 m extracted by SAM (red) revealed an age of  $1.67^{+0.0045}_{-0.0045}$ , indicating a younger age. The relatively young age of the small craters may indicate the possibility of local resurfacing events around the landing area. However, further investigation of the geological and geomorphological features of the region on a larger scale is needed to determine the nature of these resurfacing events. This study aligns with the results of some previous research [34,47–49].

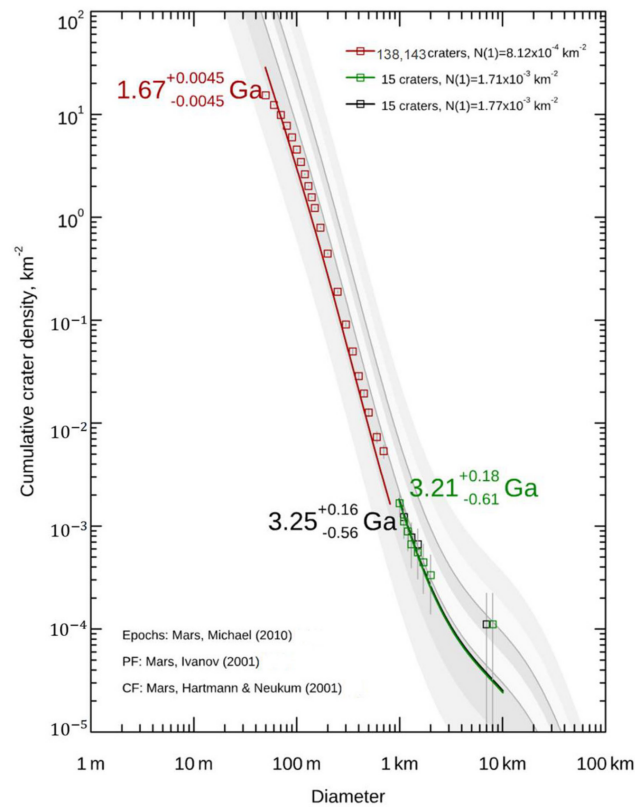


**Figure 14.** Craters' size–frequency distribution and estimation of the age of the landing area. Craters with diameters greater than 1 km, black; diameters ranging from 50 to 800 m, red; estimation of the age using the RH\_2012 dataset, green [5,44,46].

#### 4.3. Documentation of the Crater Catalog

We compiled the extracted craters from the landing area of the Tianwen-1 mission into a comprehensive catalog of craters within the landing zone. A detailed description of the data contained in this crater catalog is provided in Table 6. This table provides an example of a crater, originating from the fifth region of the landing zone's DIM, with a diameter of approximately 19.62 m. Its coordinates are approximately (25.45°N, 110.44°E). The pixel coordinates relative to the entire landing zone DIM are approximately (52,881.7, 48,093.1), and relative to the DIM of the fifth region of the landing area, the pixel coordinates are approximately (24,298.7, 5224.1).

**Table 6.** Documentation of the crater catalog.

Index	Meaning	Example
ID	Representing the region in the DIM	HX1_GRAS_HIRIC_DIM_0.7_0005_251515N1101905E_A
Latitude (degrees)	Longitude of the crater's center	25.445545541679884
Longitude (degrees)	Latitude of the crater's center	110.4361572920686
Global_x_center	X-coordinate of the center of the crater relative to the entire landing zone's DIM (in pixels)	52,881.735497283
Global_y_center	Y-coordinate of the center of the crater relative to the entire landing zone's DIM (in pixels)	48,093.05926101379
Local_x_center	X-coordinate of the center of the crater relative to the local landing area's DIM (in pixels)	24,298.735497283
Local_y_center	Y-coordinate of the center of the crater relative to the local landing area's DIM (in pixels)	5224.059261013788
Diameter (km)	Diameter of the crater	0.0196223768624538

## 5. Discussion

The current approach for extracting craters based on SAM can essentially capture all craters in the DIM, but there are still some issues that need discussion and improvement. Firstly, during the process of crater extraction, we only identified masks with a circular shape as craters. However, craters may undergo a series of geological processes, such as erosion, deposition, and reshaping, resulting in irregular shapes, as seen in the crater in Figure 15a. These craters are detected by SAM, but they may be overlooked during the process of filtering out non-circular ones, indicating that relying solely on the geometric property of circularity is not enough. The diversity in craters' morphology demands the development of more sophisticated recognition algorithms that can identify and process craters with various irregular shapes, including those shaped irregularly due to their impact angles, geological processes, or erosion.

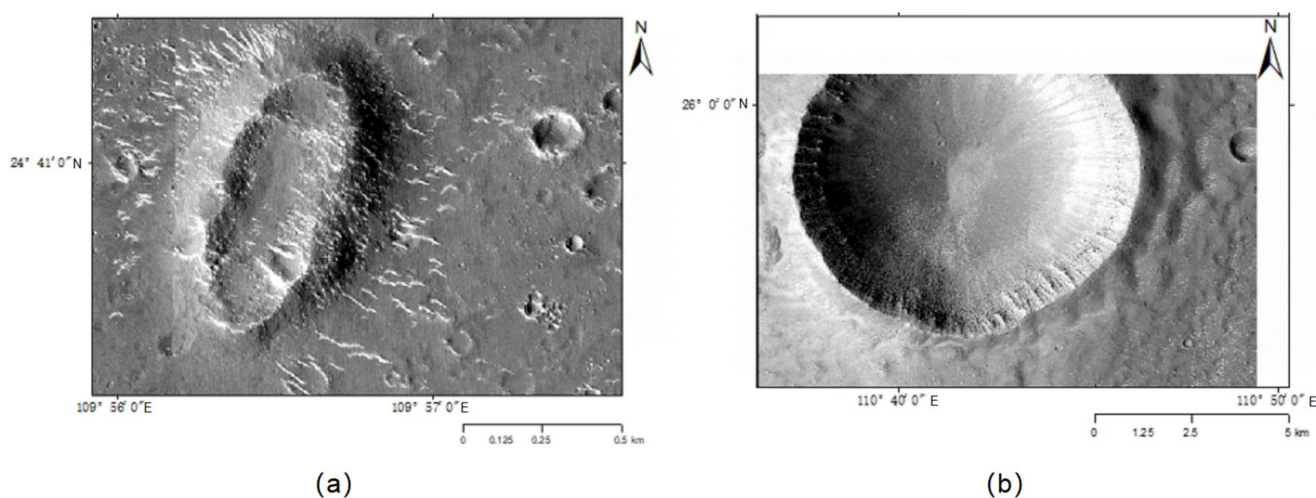


**Figure 15.** Morphological analysis of undetected craters: (a) irregularly shaped craters; (b) overlooked large-sized craters.

In addition, there was a case where the large crater in Figure 15b was not successfully extracted. The diameter of this crater is approximately 9.4 km, corresponding to a pixel diameter of 13,428. The cropping process did not fully encompass this crater, and its substantial area in the cropped image resulted in reduced contrast between the target and the background, making the extraction challenging. However, these types of craters exhibited clear features in the digital elevation model (DEM), and the resolution of the DEM was relatively lower than that of the DIM. This provides a significant advantage for detecting large-sized craters. In the subsequent steps, we will use a crater automatic extraction model based on the DEM to extract these potentially overlooked large-sized craters from the landing area's DEM.

## 6. Conclusions

This article presents a comprehensive solution for automatic crater recognition based on the Segment Anything Model (SAM), aiming to extract craters in the DIM of the landing area of the Tianwen-1 mission. We utilized SAM to obtain segmentation masks for the craters and used a series of postprocessing steps, including non-circular filtering, circular fitting, deduplication, and removal of false positives, to extract the positions and sizes of craters. Experimental validation demonstrated the effectiveness of SAM in planetary crater identification tasks. In the DIM of the Tianwen-1 landing area, we extracted a total of 841,727 craters with diameters ranging from 1.57 m to 7910.47 m, providing a comprehensive crater dataset that contributes valuable data for future missions of detecting Martian crater detection. The distribution of the number of craters reflected the geological structure and characteristics of historical impact events in the Tianwen-1 landing area.

Additionally, through the craters' size–frequency distribution, we estimated the specific surface age of the landing area to be ~3.25 billion years, with subsequent surface resurfacing events occurring ~1.67 billion years ago.

In future work, we plan to further optimize and improve the crater extraction solution using SAM. This involves optimizing postprocessing algorithms for crater extraction by considering the diversity of craters. In addition, we also plan to explore the use of multi-source data fusion techniques for crater extraction, aiming to obtain more comprehensive and accurate information on craters. Multi-source data fusion techniques can integrate data from different sensors and observation platforms, providing more comprehensive information on craters' feature. This not only enhances the accuracy and reliability of our existing models but also offers richer data support for scientific research. Furthermore, we plan to expand and improve the existing crater dataset, which will be crucial for future Martian exploration and research. Finally, we hope to apply these techniques to the study of craters on other celestial bodies such as the Moon, asteroids, etc., to further extend the reach of our research and provide more data and insights for the geological study of these celestial bodies. Through these efforts, we aim to offer more comprehensive and in-depth support for the geological exploration and research of Mars and other celestial bodies.

**Author Contributions:** Conceptualization, H.Y.; methodology, Y.Z.; writing, Y.Z.; supervision, H.Y. All authors have read and agreed to the published version of the manuscript.

**Funding:** This work was funded by the National Natural Science Foundation of China, grant 62271152.

**Data Availability Statement:** The extracted crater dataset is available at [https://drive.google.com/file/d/1pKRIC0Zh2fe1taZcFpwB-QysfxXy2doi/view?usp=drive\\_link](https://drive.google.com/file/d/1pKRIC0Zh2fe1taZcFpwB-QysfxXy2doi/view?usp=drive_link) (accessed on 1 May 2024).

**Conflicts of Interest:** The authors declare no conflicts of interest.

## References

- Meng, Q.; Wang, D.; Wang, X.; Li, W.; Yang, X.; Yan, D.; Li, Y.; Cao, Z.; Ji, Q.; Sun, T.; et al. High Resolution Imaging Camera (HiRIC) on China's First Mars Exploration Tianwen-1 Mission. *Space Sci. Rev.* **2021**, *217*, 42. [CrossRef]
- Head, J.W., 3rd; Fassett, C.I.; Kadish, S.J.; Smith, D.E.; Zuber, M.T.; Neumann, G.A.; Mazarico, E. Global distribution of large lunar craters: Implications for resurfacing and impactor populations. *Science* **2010**, *329*, 1504–1507. [CrossRef] [PubMed]
- Hu, T.; Yang, Z.; Kang, Z.; Lin, H.; Zhong, J.; Zhang, D.; Cao, Y.; Geng, H. Population of Degrading Small Impact Craters in the Chang'E-4 Landing Area Using Descent and Ground Images. *Remote Sens.* **2022**, *14*, 3608. [CrossRef]
- Wu, B.; Huang, J.; Li, Y.; Wang, Y.; Peng, J. Rock Abundance and Crater Density in the Candidate Chang'E-5 Landing Region on the Moon. *J. Geophys. Res. Planets* **2018**, *123*, 3256–3272. [CrossRef]
- Hartmann, W.K.; Neukum, G. Cratering chronology and the evolution of Mars. In *Chronology and Evolution of Mars: Proceedings of an ISSI Workshop, Bern, Switzerland, 10–14 April 2000*; Springer Netherlands: Dordrecht, The Netherlands, 2001; pp. 165–194.
- Neukum, G. Meteoritenbombardement und Datierung Planetarer Oberflachen. Habilitation Dissertation, Faculty Membership, Ludwig-Maximilians-University, Munchen, Germany, 1983.
- Povilaitis, R.Z.; Robinson, M.S.; van der Bogert, C.H.; Hiesinger, H.; Meyer, H.M.; Ostrach, L.R. Crater density differences: Exploring regional resurfacing, secondary crater populations, and crater saturation equilibrium on the moon. *Planet. Space Sci.* **2018**, *162*, 41–51. [CrossRef]
- Cheng, Y.; Johnson, A.E.; Matthies, L.H.; Olson, C.F. Optical landmark detection for spacecraft navigation. In Proceedings of the 13th Annual AAS/AIAA Space Flight Mechanics Meeting, Ponce, Puerto Rico, 9–13 February 2003; pp. 1–19.
- Illingworth, J.; Kittler, J. A survey of the Hough transform. *Comput. Vis. Graph. Image Process.* **1988**, *44*, 87–116. [CrossRef]
- Briechele, K.; Hanebeck, U.D. Template matching using fast normalized cross correlation. *Proc. SPIE Int. Soc. Opt. Eng.* **2001**, *4387*, 1–8.
- Leroy, B.; Medioni, G.; Johnson, E.; Matthies, L. Crater detection for autonomous landing on asteroids. *Image Vis. Comput.* **2001**, *19*, 787–792. [CrossRef]
- Galloway, M.J.; Benedix, G.K.; Bland, P.A.; Paxman, J.; Towner, M.C.; Tan, T. Automated crater detection and counting using the Hough transform. In Proceedings of the 2014 IEEE International Conference on Image Processing (ICIP), Paris, France, 27–30 October 2014; pp. 1579–1583.
- Dong, S.; Wang, L.; Du, B.; Meng, X. ChangeCLIP: Remote sensing change detection with multimodal vision-language representation learning. *ISPRS J. Photogramm. Remote Sens.* **2024**, *208*, 53–69. [CrossRef]
- Li, Y.; Du, L.; Wei, D. Multiscale CNN Based on Component Analysis for SAR ATR. *IEEE Trans. Geosci. Remote Sens.* **2022**, *60*, 5211212. [CrossRef]

15. Li, J.; Chen, K.; Tian, G.; Li, L.; Shi, Z. MarsSeg: Mars Surface Semantic Segmentation with Multi-level Extractor and Connector. *arXiv* **2024**, arXiv:2404.04155.
16. Silburt, A.; Ali-Dib, M.; Zhu, C.; Jackson, A.; Valencia, D.; Kissin, Y.; Tamayo, D.; Menou, K. Lunar crater identification via deep learning. *Icarus* **2019**, *317*, 27–38. [[CrossRef](#)]
17. Speyerer, E.; Robinson, M.; Denevi, B.; Team, L.S. Lunar Reconnaissance Orbiter Camera Global Morphological Map of the Moon. In Proceedings of the 42nd Annual Lunar and Planetary Science Conference, The Woodlands, TX, USA, 7–11 March 2011; p. 2387.
18. Ronneberger, O.; Fischer, P.; Brox, T. U-net: Convolutional networks for biomedical image segmentation. In *Medical Image Computing and Computer-Assisted Intervention—MICCAI 2015, Proceedings of the 18th International Conference, Munich, Germany, 5–9 October 2015*; Proceedings, Part III; Springer International Publishing: Berlin/Heidelberg, Germany, 2015; pp. 234–241.
19. Lee, C. Automated crater detection on Mars using deep learning. *Planet. Space Sci.* **2019**, *170*, 16–28. [[CrossRef](#)]
20. Chen, D.; Hu, F.; Mathiopoulos, P.T.; Zhang, Z.; Peethambaran, J. MC-UNet: Martian Crater Segmentation at Semantic and Instance Levels Using U-Net-Based Convolutional Neural Network. *Remote Sens.* **2023**, *15*, 266. [[CrossRef](#)]
21. Zhao, Y.; Ye, H. SqUNet: An High-Performance Network for Crater Detection With DEM Data. *IEEE J. Sel. Top. Appl. Earth Obs. Remote Sens.* **2023**, *16*, 8577–8585. [[CrossRef](#)]
22. Yang, C.; Zhao, H.; Bruzzone, L.; Benediktsson, J.A.; Liang, Y.; Liu, B.; Zeng, X.; Guan, R.; Li, C.; Ouyang, Z. Lunar impact crater identification and age estimation with Chang'E data by deep and transfer learning. *Nat. Commun.* **2020**, *11*, 6358. [[CrossRef](#)]
23. Robbins, S.J.; Hynek, B.M. A new global database of Mars impact craters  $\geq 1$  km: 1. Database creation, properties, and parameters. *J. Geophys. Res. Planets* **2012**, *117*. [[CrossRef](#)]
24. Jia, M.; Yue, Z.; Di, K.; Liu, B.; Liu, J.; Michael, G. A catalogue of impact craters larger than 200 m and surface age analysis in the Chang'e-5 landing area. *Earth Planet. Sci. Lett.* **2020**, *541*, 116272. [[CrossRef](#)]
25. Chen, K.; Liu, C.; Chen, H.; Zhang, H.; Li, W.; Zou, Z.; Shi, Z. RSPrompter: Learning to prompt for remote sensing instance segmentation based on visual foundation model. *IEEE Trans. Geosci. Remote Sens.* **2024**, *62*, 4701117. [[CrossRef](#)]
26. Kirillov, A.; Mintun, E.; Ravi, N.; Mao, H.; Rolland, C.; Gustafson, L.; Xiao, T.; Whitehead, S.; Berg, A.C.; Lo, W.-Y. Segment anything. *arXiv* **2023**, arXiv:2304.02643.
27. Mazurowski, M.A.; Dong, H.; Gu, H.; Yang, J.; Konz, N.; Zhang, Y. Segment anything model for medical image analysis: An experimental study. *Med. Image Anal.* **2023**, *89*, 102918. [[CrossRef](#)]
28. Giannakis, I.; Bhardwaj, A.; Sam, L.; Leontidis, G. A flexible deep learning crater detection scheme using Segment Anything Model (SAM). *Icarus* **2024**, *408*, 115797. [[CrossRef](#)]
29. Wan, W.X.; Wang, C.; Li, C.L.; Wei, Y. China's first mission to Mars. *Nat. Astron.* **2020**, *4*, 721. [[CrossRef](#)]
30. Niu, S.; Zhang, F.; Di, K.; Gou, S.; Yue, Z. Layered Ejecta Craters in the Candidate Landing Areas of China's First Mars Mission (Tianwen-1): Implications for Subsurface Volatile Concentrations. *J. Geophys. Res. Planets* **2022**, *127*, e2021JE007089. [[CrossRef](#)]
31. Zhao, J.; Xiao, Z.; Huang, J.; Head, J.W.; Wang, J.; Shi, Y.; Wu, B.; Wang, L. Geological Characteristics and Targets of High Scientific Interest in the Zhurong Landing Region on Mars. *Geophys. Res. Lett.* **2021**, *48*, e2021GL094903. [[CrossRef](#)]
32. Wu, B.; Dong, J.; Wang, Y.; Li, Z.; Chen, Z.; Liu, W.C.; Zhu, J.; Chen, L.; Li, Y.; Rao, W. Characterization of the Candidate Landing Region for Tianwen-1—China's First Mission to Mars. *Earth Space Sci.* **2021**, *8*, e2021EA001670. [[CrossRef](#)]
33. Wu, X.; Liu, Y.; Zhang, C.; Wu, Y.; Zhang, F.; Du, J.; Liu, Z.; Xing, Y.; Xu, R.; He, Z.; et al. Geological characteristics of China's Tianwen-1 landing site at Utopia Planitia, Mars. *Icarus* **2021**, *370*, 114657. [[CrossRef](#)]
34. Wu, B.; Dong, J.; Wang, Y.; Rao, W.; Sun, Z.; Li, Z.; Tan, Z.; Chen, Z.; Wang, C.; Liu, W.C.; et al. Landing Site Selection and Characterization of Tianwen-1 (Zhurong Rover) on Mars. *J. Geophys. Res. Planets* **2022**, *127*, e2021JE007137. [[CrossRef](#)]
35. Cao, Z.; Kang, Z.; Hu, T.; Yang, Z.; Zhu, L.; Ye, C. Cross-attention induced multilayer domain adaptation network for extraction of sub-kilometer craters from HiRIC images. *Icarus* **2024**, *407*, 115776. [[CrossRef](#)]
36. Dosovitskiy, A.; Beyer, L.; Kolesnikov, A.; Weissenborn, D.; Zhai, X.; Unterthiner, T.; Dehghani, M.; Minderer, M.; Heigold, G.; Gelly, S. An image is worth 16x16 words: Transformers for image recognition at scale. *arXiv* **2020**, arXiv:2010.11929.
37. Vaswani, A.; Shazeer, N.; Parmar, N.; Uszkoreit, J.; Jones, L.; Gomez, A.N.; Kaiser, Ł.; Polosukhin, I. Attention is all you need. *Adv. Neural Inf. Process. Syst.* **2017**, *30*, 600–610.
38. Mordvintsev, A.; Abid, K. Opencv-Python Tutorials Documentation. 2014. Available online: <https://buildmedia.readthedocs.org/media/pdf/opencv-python/latest/opencv-python.pdf> (accessed on 10 January 2024).
39. Bottema, M.J. Circularity of objects in images. In Proceedings of the 2000 IEEE International Conference on Acoustics, Speech, and Signal Processing (Cat. No. 00CH37100), Istanbul, Turkey, 5–9 June 2000; pp. 2247–2250.
40. Gou, S.; Yue, Z.; Di, K.; Zhao, C.; Bugiolacchi, R.; Xiao, J.; Cai, Z.; Jin, S. Transverse aeolian ridges in the landing area of the Tianwen-1 Zhurong rover on Utopia Planitia, Mars. *Earth Planet. Sci. Lett.* **2022**, *595*, 117764. [[CrossRef](#)]
41. Wang, S.; Fan, Z.; Li, Z.; Zhang, H.; Wei, C. An effective lunar crater recognition algorithm based on convolutional neural network. *Remote Sens.* **2020**, *12*, 2694. [[CrossRef](#)]
42. Jia, Y.; Liu, L.; Zhang, C. Moon impact crater detection using nested attention mechanism based UNet++. *IEEE Access* **2021**, *9*, 44107–44116. [[CrossRef](#)]
43. Grant, J.A.; Schultz, P.H. Degradation of selected terrestrial and Martian impact craters. *J. Geophys. Res. Planets* **1993**, *98*, 11025–11042. [[CrossRef](#)]
44. Ivanov, B.A. Mars/Moon cratering rate ratio estimates. *Space Sci. Rev.* **2001**, *96*, 87–104. [[CrossRef](#)]

45. Neukum, G.; Ivanov, B.A.; Hartmann, W.K. Cratering records in the inner solar system in relation to the lunar reference system. In *Chronology and Evolution of Mars, Proceedings of an ISSI Workshop, Bern, Switzerland, 10–14 April 2000*; Springer: Dordrecht, The Netherlands, 2001; pp. 55–86.
46. Michael, G.; Neukum, G. Planetary surface dating from crater size–frequency distribution measurements: Partial resurfacing events and statistical age uncertainty. *Earth Planet. Sci. Lett.* **2010**, *294*, 223–229. [[CrossRef](#)]
47. Tanaka, K.L.; Skinner, J.A., Jr.; Dohm, J.M.; Irwin, R.P., III; Kolb, E.J.; Fortezzo, C.M.; Platz, T.; Michael, G.G.; Hare, T.M. *Geologic Map of Mars*; U.S. Geological Survey: Reston, VA, USA, 2014; p. 3292. [[CrossRef](#)]
48. Ivanov, M.A.; Hiesinger, H.; Erkeling, G.; Reiss, D. Mud volcanism and morphology of impact craters in Utopia Planitia on Mars: Evidence for the ancient ocean. *Icarus* **2014**, *228*, 121–140. [[CrossRef](#)]
49. Huang, H.; Wang, X.; Chen, Y.; Zhang, Q.; Zhao, F.; Ren, X.; Zeng, X.; Yan, W.; Chen, W.; Liu, B. Observations and interpretations of geomorphologic features in the Tianwen-1 landing area on Mars by using orbital imagery data. *Earth Planet. Phys.* **2022**, *7*, 331–346. [[CrossRef](#)]

**Disclaimer/Publisher’s Note:** The statements, opinions and data contained in all publications are solely those of the individual author(s) and contributor(s) and not of MDPI and/or the editor(s). MDPI and/or the editor(s) disclaim responsibility for any injury to people or property resulting from any ideas, methods, instructions or products referred to in the content.